1 # A novel formation mechanism of sulfamic acid and its enhancing

2 # effect on methanesulfonic acid-methylamine aerosol particle

3 # formation in agriculture-developed and coastal industrial areas

4 **Hui Wang [a,‡], Shuqin Wei [a,‡], Jihuan Yang [a], Yanlong Yang [a], Rongrong Li [a], Rui Wang [a],**

5 **Chongqin Zhu [b,*], Tianlei Zhang [a,*], Changming Zhang [c]**

6 [a] *Shaanxi Key Laboratory of Catalysis, School of Chemical & Environment Science, Shaanxi*
7 *University of Technology, Hanzhong, Shaanxi 723001, P. R. China*
8 [b] *College of Chemistry, Key Laboratory of Theoretical & Computational Photochemistry of*
9 *Ministry of Education, Beijing Normal University, Beijing 100190, China.*
10 [c] *School of Mechanical Engineering, Shaanxi University of Technology, Hanzhong, Shaanxi 723001,*
11 *P. R. China*

12 ## Abstract

13 Sulfamic acid (SFA) significantly impacts atmospheric pollution and poses potential risks to human
14 health. Although traditional source of SFA and its role on sulfuric acid-dimethylamine new particle
15 formation (NPF) has received increasing attention, the formation mechanism of SFA from $HNSO_2$
16 hydrolysis with methanesulfonic acid (MSA) and its enhancing effect on MSA-methylamine (MA)
17 NPF has not been studied, which will limit the understanding for the source and loss of SFA in
18 agriculture-developed and coastal industrial areas. Here, the gaseous and interfacial formation of
19 SFA from $HNSO_2$ hydrolysis with MSA was investigated using quantum chemical calculations and
20 BOMD simulations. Furthermore, the role of SFA in MSA-MA system was assessed using the
21 ACDC kinetic model. Our simulation results indicate that the gaseous SFA formation from the
22 hydrolysis of $HNSO_2$ with MSA can be competitive with that catalyzed by H_2O within an altitude
23 of 5-15 km. At the air-water interface, two types of reactions, the ions forming mechanism and the
24 proton exchange mechanism to form $SFA^-\cdots H_3O^+$ ion pair were observed on the timescale of
25 picosecond. Considering the overall environment of sulfuric acid emission reduction, the present
26 findings suggest that SFA may play a significant role in NPF and the growth of aerosol particle as
27 *i*) SFA can directly participate in the formation of MSA-MA-based cluster and enhance the rate of
28 NPF from these clusters by approximately 10^3 times at 278.15 K; and *ii*) the SFA^- species at the air-
29 water interface can attract gaseous molecules to the aqueous surface, and thus promote particle
30 growth.

* Corresponding authors, Tel: +86-0916-2641083, Fax: +86-0916-2641083.
E-mail: cqzhu@bnu.edu.cn (C. Q. Zhu), ztianlei88@l63.com (T. L. Zhang).
‡ These authors contributed equally to this work.

1 Introduction

As a well-studied nitrogen derivative of sulfuric acid (Rennebaum et al., 2024), sulfamic acid (SFA) was not only recognized as a potent aerosol and cloud nucleating agent (Xue et al., 2024; Zhang et al., 2023; Pszona et al., 2015; Li et al., 2018), but also can harm human health through atmospheric deposition into water bodies (Van Stempvoort et al., 2019). In agriculture-developed and industrial areas with high ammonia (NH_3) concentrations, such as the Yangtze River Delta in China (Yu et al., 2020), Indo-Gangetic Plains (Kuttippurath et al., 2020), Pakistan, Bangladesh (Warner et al., 2016), and the southern Italy (Tang et al., 2021), the atmospheric concentration of SFA estimated by theoretical method of CCSD(T)-F12/cc-pVDZ-F12//M06-2X/6-311++G(3df,3pd) (Li et al., 2018) was expected to reach up to 10^8 molecules·cm^{-3}, and thus lead to it becoming a significant air pollutant. So, the sources of SFA in the atmosphere has been focused by several groups (Lovejoy and Hanson, 1996; Pszona et al., 2015; Li et al., 2018; Larson and Tao, 2001; Manonmani et al., 2020; Zhang et al., 2022). The traditional source of SFA was mainly taken from the ammonolysis of SO_3 (Lovejoy and Hanson, 1996; Larson and Tao, 2001; Li et al., 2018). Experimentally, the rate coefficient for the ammonolysis of SO_3 was detected to be 2.0×10^{-11} cm^3·$molecules^{-1}$·s^{-1} at 295 K (Lovejoy and Hanson, 1996), which was close to the value for the hydrolysis of SO_3 assisted by water molecule (10^{-11}-10^{-10} cm^3 $molecule^{-1}$ s^{-1}) (Kim et al., 1998; Hirota et al., 1996; Shi et al., 1994; Kolb et al., 1994; Long et al., 2013; Long et al., 2023; Ding et al., 2023; Cheng et al., 2023; Wang et al., 2024). Theoretically, the ammonolysis of SO_3 to produce SFA can be catalyzed by NH_3. In arid and heavily polluted regions with high NH_3 concentrations, the effective rate coefficient for the ammonolysis of SO_3 can be sufficiently rapid, making it competitive with the conventional loss pathway of SO_3 with water (Li et al., 2018).

In addition to the ammonolysis of SO_3, new sources of SFA formation have received increasing attention (Zhang et al., 2022; Manonmani et al., 2020, Li et al., 2018, Xue et al., 2024). The existence of $HNSO_2$ was proposed in the reaction between SO_3 and NH_3, and was regarded as the most stable for nine different isomers of $HNSO_2$, HONSO, HOSNO, HOS(O)N, $HSNO_2$, HSONO, HON(O)S, HOOSN, and HOONS (Deng et al., 2016). Owing to its similarity with SO_3 and the potential role of SO_3 in the atmosphere, the hydrolysis of $HNSO_2$ to produce SFA formation has been focused by several groups (Zhang et al., 2022; Manonmani et al., 2020). As the direct

60   hydrolysis of $HNSO_2$ with a high energy barrier takes place hardly in the gas phase (Zhang et al.,

61   2022; Manonmani et al., 2020), the addition of a second water molecule (Manonmani et al., 2020),

62   formic acid and sulfuric acid (H_2SO_4, SA) (Zhang et al., 2022) have been proved to promote the

63   product of SFA through the hydrolysis of $HNSO_2$. It was noted that, with the global reduction in the

64   concentration of H_2SO_4 resulting from SO_2 emission restrictions, the contribution of

65   methanesulfonic acid (MSA) to aerosol nucleation has received the widespread attention of

66   scientists. As a major inorganic acidic air pollutant (Chen et al., 2020), the concentration of MSA

67   in the atmosphere was noted to be notably high across various regions, spanning from coastal to

68   continental, with levels found to be between 10% and 250% of those measured for SA (Shen et al.,

69   2019; Dawson et al., 2012; Bork et al., 2014; Shen et al., 2020; Berresheim et al., 2002; Hu et al.,

70   2023). However, to the best of our knowledge, the gaseous hydrolysis of $HNSO_2$ with MSA has not

71   yet been investigated, which will confine the understanding for the source of SFA in regions with

72   significant pollution and high levels of MSA. Thus, understanding the hydrolysis of $HNSO_2$ with

73   MSA in the gas phase was necessary for exploring its impact on aerosols and human health.

74    $$HNSO_2 + H_2O + MSA \rightarrow SFA + MSA \tag{1}$$
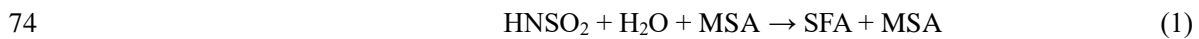
75   As a supplement to gas-phase reactions, interfacial reactions at the air-water interface not only

76   can accelerate the rates of atmospheric reactions but also may introduce new mechanisms (Freeling

77   et al., 2020; Zhong et al., 2019). For instance, the Criegee intermediates reacting with MSA at the

78   air-water interface can form the ion pair of $CH_3C(H)(OOH)(SO_3CH_3)$ anhydride and H_3O^+ (Ma et

79   al., 2020), which differs from the corresponding gaseous reaction where the MSA molecule acts

80   solely as a reactant reacting with Criegee intermediates directly. As far as we know, $HNSO_2$ exhibit

81   a significant interfacial preference, as the fact that the total duration time of $HNSO_2$ at the interface

82   approximately accounts for 49.1% of the 150 ns simulation time (Fig. S1). However, the hydrolysis

83   of $HNSO_2$ with MSA has not been studied at the air-water interface, which will limit our

84   understanding of how the hydrolysis of $HNSO_2$ with MSA differs in the gas phase and air-water

85   interfaces.

86   From a structural point of view, two functional groups of $-NH_2$ and $-SO_3H$ in the SFA molecule

87   can act as both hydrogen donors and acceptors to interact with atmospheric species. Previous studies

88   have demonstrated that SFA has a potential role in new particle formation (NPF), as it not only

89   clusters efficiently with itself and SA (Lovejoy and Hanson, 1996), but also can promote the

90   nucleation rate of NPF initiated from SA-DMA by a factor of two in dry and severely contaminated

91   areas with NH_3 (Li et al., 2018). Due to the concentration of SA in the atmosphere has decreased

92   significantly with the scenario of SO_2 emission control measures, MSA-driven NPF has attracted

93   growing attention (Dawson et al., 2012; Nishino et al., 2014; Chen and Finlayson-Pitts, 2017; Chen

94   et al., 2020; Shen et al., 2020). Initially, the binary nucleation of MSA with inorganic ammonia and

95   organic amines in the atmosphere has been reported, where MA exhibits the strongest enhancing

96   capability (Chen et al., 2016; Chen and Finlayson-Pitts, 2017; Shen et al., 2019; Hu et al., 2023).

97   Subsequently, some reported results suggested that the triadic MSA-MA-driven NPF can exhibit

98   greater nucleation rates competed to the binary of MSA-driven (Zhang et al., 2022: Hu et al., 2023).

99   For example, both formic acid (Zhang et al., 2022) and trifluoroacetic acid (Hu et al., 2023) exhibit

100 an excellent catalytic influence on MSA-MA-driven NPF. However, the SFA involved in MSA-

101 MA-driven NPF has not been investigated, which is worth important to investigate whether SFA

102 can exhibit a similar enhancing effect in MSA-MA as observed in SA-DMA.

103 Herein, this work studied the catalytic effect of SFA on $HNSO_2$ hydrolysis and MSA-MA

104 nucleation particle formation. Specifically, quantum chemical calculations were used firstly to

105 assess the atmospheric processes of the gaseous hydrolysis of $HNSO_2$ with MSA. Then, the gaseous

106 and interfacial mechanisms differences of the $HNSO_2$ hydrolysis with MSA were investigated

107 applying the Born-Oppenheimer Molecular Dynamic (BOMD) simulation method. Finally, the

108 atmospheric implications and mechanism of SFA in the MSA-MA-dominated NPF process have

109 been evaluated through density functional theory and the Atmospheric Clusters Dynamic Code

110 (ACDC) (McGrath et al., 2012; Hu et al., 2023; Zhao et al., 2020; Zhang et al., 2024; Tsona Tchinda

111 et al., 2022; Liu et al., 2020) models to evaluate the potential effect of SFA on nucleation and NPF.

112 This work will not only deepen our understanding of the source of SFA, but also reveal significant

113 implications for new particle formation and aerosol particle growth in MSA polluted areas.

2   Methodology

2.1 Quantum Chemical Calculations

116 The gaseous hydrolysis of $HNSO_2$ with MSA was comprehensively studied through quantum

117 chemistry simulations. Optimization of all the species were carried out by using the method of M06-

118 2X with 6-311++G($2df$,$2pd$) basis set (Zhao and Truhlar, 2008; Elm et al., 2012; Bork et al., 2014).

119 Vibrational frequencies were subsequently computed at the M06-2X/6-311++G(2df,2pd) level to

120 ensure the reality of all stationary point's frequencies and the presence of only one imaginary

121 frequency in transition states. It is noted that the calculated bond distances and bond angles at the

122 M06-2X/6-311++G(2df,2pd) level (Fig. S2) agree well with the available values (Fig. S2) from the

123 experiment and three different theoretical levels of M06-2X/6-311++G(3df,2pd), M062X/6-

124 311++G(3df,3pd) and M06-2X/aug-cc-pVTZ levels. Also, at the M06-2X/6-311++G(2df,2pd) level,

125 internal reaction coordinate (IRC) analyses were conducted to verify the connection from the

126 transition states to the corresponding products (or reactants). All calculations regarding for

127 geometries and frequency were conducted with the aid of the Gaussian 09 (Frisch, 2009) program.

128 Furthermore, single point energies were performed at the CCSD(T)-F12/cc-pVDZ-F12 (Kendall et

129 al., 1992; Adler et al., 2007) level utilizing the ORCA (Neese, 2012) program, based on the

130 optimized geometries mentioned above. The CCSD(T)/aug-cc-pVDZ method was chosen to

131 calculate the relative energies as the fact that, compared with unsigned error (Table S1) calculated

132 at the CCSD(T)/CBS//M06-2X/6-311++G(2df,2pd) level, unsigned errors calculated at CCSD(T)-

133 F12/cc-pVDZ-F12//M06-2X/6-311++G(2df,2pd) was 0.71 kcal·mol^{-1}.

134 **2.2 Rate coefficients calculations**

135 The rate coefficients for the hydrolysis of HNSO$_2$ with MSA were calculated through a two-

136 step process. Initially, the high-pressure-limit (HPL) rate coefficients were computed applying

137 VRC-VTST methods within the Polyrate package (Chuang et al., 1999). It's worth noting that the

138 electronic structure method for VRC-TST calculations is based on Gaussian 09 program using the

139 M06-2X/6-311++G(2df,2pd). Meanwhile, two pivot points were selected (Bao et al., 2016; Long et

140 al., 2021; Georgievskii and Klippenstein, 2003; Meana-Pañeda et al., 2024) to produce a single-

141 faceted dividing surface for the HNSO$_2$ hydrolysis (shown in Part S1 in the Supplement).

142 Subsequently, on the basis of the HPL rate coefficients, the rate coefficients for the hydrolysis of

143 HNSO$_2$ with MSA were calculated within the temperature range of 212.6-320.0 K and pressures

144 applying the Master Equation Solver for Multi-Energy Well Reactions (MESMER) program

145 (Glowacki et al., 2012). The rate coefficients for the barrierless steps transitioning between reactants

146 and pre-reactive complexes were assessed applying the Inverse Laplace Transform (ILT) method

147 within MESMER calculations, while the step transitioning between pre-reactive complexes and

148 post-reactive complexes via transition states were evaluated using the RRKM theory (Mai et al.,

149 2018) in combination with the asymmetric Eckart model. The details of the rate coefficient for the

150 hydrolysis of $HNSO_2$ without and with X ($X = H_2O$ and MSA) were given in Part 1, Table 1 and

151 Table S4.

2.3 BOMD Simulations

153 BOMD simulations were conducted applying DFT implemented in CP2K program

154 (Vandevondele et al., 2005; Hutter et al., 2014). The exchange and correlation interactions were

155 addressed using the Becke-Lee-Yang-Parr (BLYP) functional (Becke, 1988; Lee et al., 1988),

156 while Grimme's dispersion was applied to address weak dispersion interaction (Grimme et al.,

157 2010). The Goedecker-Teter-Hutter (GTH) conservation pseudopotential (Goedecker et al.,

158 1996; Hartwigsen et al., 1998) combine with Gaussian DZVP basis set (Vandevondele and

159 Hutter, 2007) and an auxiliary plane wave basis set were used to represent core and valence

160 electrons. Energy cutoffs (Zhong et al., 2017; Zhong et al., 2018; Zhong et al., 2019) of 280 Ry

161 for the plane wave basis set and 40 Ry for the Gaussian basis set were applied. The gaseous

162 reactions were simulated in the NVT ensemble at 300 K, with $15 \times 15 \times 15$ Å^3 supercells and the

163 time step of 1 fs. To simulate the water microdroplet, the system containing 191 water molecules

164 (Zhong et al., 2017) was utilized in $35 \times 35 \times 35$ Å^3 supercells. This setup included $HNSO_2$ and

165 MSA along with the water drop. Prior to the interfacial simulation, a 10 ps relaxation period in

166 the BOMD simulation was used to equilibrate the water microdroplet system with 191

167 molecules.

2.4 ACDC kinetics simulation

169 The ACDC model (McGrath et al., 2012; Hu et al., 2023; Zhao et al., 2020; Zhang et al., 2024;

170 Tsona Tchinda et al., 2022; Liu et al., 2020) was utilized to simulate the $(MSA)_x(MA)_y(SFA)_z$ (0

171 $\leq y \leq x + z \leq 3$) cluster formation rates and explore the potential mechanisms, where the most

172 stable structure of $(SFA)_x(MSA)_y(MA)_z$ ($0 \leqslant z \leqslant x + y \leqslant 3$) clusters were searched with

173 ABCluster software (Zhang and Dolg, 2015) (The details in Part S1 of the Supplement). This

174 simulation encompasses a variety of temperatures and monomer concentrations to capture the

175 dynamics under different environmental conditions. Thermodynamic parameters, obtained from

176 quantum chemical calculations executed at the M06-2X/6-311++G($2df,2pd$) level, were used

177 as inputs for the ACDC model. Notably, many benchmark studies (Zhao et al., 2020; Zhang et al.,

178 2024; Tsona Tchinda et al., 2022; Liu et al., 2020) show that the M06-2X functional has good

179　performance compared to other common functionals for gaining the Gibbs free energies. For all the

180　M06-2X calculations with the 6-311++G(2*df*,2*pd*) basis set was used, as it is a good compromise

181　between accuracy and efficiency and does not yield significant errors in the thermal contribution to

182　the free energy compared to much larger basis sets such as 6-311++G(3*df*,3*pd*), with the differences

183　of relative ΔG less than 1.75 kcal·mol^{-1} (Table S7). The temporal progression of cluster

184　concentrations was determined by numerically integrating the birth-death equation, leveraging

185　MATLAB's ode15s solver for enhanced accuracy.

186
$$\frac{dc_i}{dt} = \frac{1}{2}\sum_{j<i}\beta_{j,(i-j)}c_jc_{(i-j)} + \sum_{j}\gamma_{(i+j)\to i}c_{i+j} - \sum_{j}\beta_{i,j}c_ic_j - \frac{1}{2}\sum_{j<i}\gamma_{i\to j}c_i + Q_i - S_i \quad (2)$$

187　Here, c_i represents the concentration of a specific cluster, labelled as i; the term $\beta_{i,j}$ was used to

188　denote the collision coefficient, which was a measure of the frequency at which clusters i and j

189　collide with each other in a given environment or system; the coefficient $\gamma_{(i+j)\to i}$ was defined

190　as the evaporation rate constant that describes the process of a larger cluster, consisting of

191　combined elements i and j, breaking down into the individual smaller clusters i and j; and Q_i

192　encompasses all other source terms contributing to the formation of cluster i. S_i signifies

193　alternative sink terms for cluster i that may remove it from the system. Considering the

194　formation Gibbs free energy (Table S8) and evaporation rates (Table S9) of all clusters, the

195　clusters containing pure MSA and MA molecules as well as the clusters containing a SFA

196　molecule are mostly more stable and therefore are allowed to form larger clusters and contribute

197　to particle formation rates. In this case, clusters $(MSA)_4 \cdot (MA)_3$, $(MSA)_4 \cdot (MA)_4$ and

198　$SFA \cdot (MSA)_3 \cdot (MA)_3$ are set as the boundary clusters.

3. Results and discussions

3.1 The hydrolysis of HNSO$_2$ with MSA in the gas phase

201　　　Given the low chance of three molecules of HNSO$_2$, H$_2$O and MSA colliding simultaneously

202　under atmospheric conditions, the hydrolysis of HNSO$_2$ with MSA (Channel MSA) was likely a

203　sequential bimolecular process. As the concentration of water molecule (10^{18} molecules·cm^{-3}

204　(Anglada et al., 2013)) in the atmosphere is much higher than those of HNSO$_2$ and MSA (10^5-10^9

205　molecules·cm^{-3} (Shen et al., 2020)), the reaction pathway of HNSO$_2$···MSA + H$_2$O is hard to occur

206　in actual atmospheric conditions. So, Channel MSA proceeds through the initial formation of dimers

207 (HNSO$_2$···H$_2$O and MSA···H$_2$O) via collisions between HNSO$_2$ (or MSA) and H$_2$O. Subsequently,

208 the generated dimer interacts with the third reactant, either MSA or HNSO$_2$. As seen in Fig. 1, the

209 calculated Gibbs free energy of MSA···H$_2$O complex was -0.9 kcal·mol^{-1}, which was 4.5 kcal·mol^{-1}

210 ^{1} lower than that of HNSO$_2$···H$_2$O. Consequently, it was predicted the primary route for the

211 hydrolysis reaction of HNSO$_2$ with MSA takes place via the HNSO$_2$ + MSA···H$_2$O reaction.

212 Starting from the HNSO$_2$ + MSA···H$_2$O reactants, the Channel MSA was initiated through the

213 intermediate complex designated as IM_MSA1. From a geometric perspective, IM_MSA1 complex

214 exhibits a cage-like configuration by a van der Waals force (S1···O1, 2.00 Å) and the involvement

215 of three hydrogen bonds of H2···O4 (1.53 Å), H4···N1 (1.60 Å) and H5···O3 (2.07 Å). The Gibbs

216 free energy of IM_MSA1 complex relative to HNSO$_2$ + MSA···H$_2$O reactants was 1.7 kcal·mol^{-1}.

217 Subsequently, as presented in Fig. 1, Channel MSA progresses through transition state TS_MSA1

218 to yield complex IMF_MSA1. At TS_MSA1, the MSA moiety facilitates two hydrogen atom

219 transfer, with TS_MSA1 lying only 0.8 kcal·mol^{-1} above complex IM_MSA1. Complex

220 IMF_MSA1 exhibits a cage-like structure with a Gibbs free energy was 23.4 kcal·mol^{-1} lower than

221 that of IM_MSA1, revealing thermodynamic favorability of HNSO$_2$ hydrolysis with MSA. To

222 evaluate the relative catalytic impact of MSA and H$_2$O, Fig. S4 illustrates the profiles of Gibbs free

223 energy for the hydrolysis of HNSO$_2$ and the corresponding reaction assisted by H$_2$O. Compared to

224 complex HNSO$_2$···(H$_2$O)$_2$, the Gibbs stabilization energy of IM_MSA1 increased by 5.6 kcal·mol^{-1}

225 ^{1}, potentially shortening the S1···O1 bond distance by 0.21 Å. Considering the Gibbs free energy

226 barrier and rate coefficients, MSA demonstrates a greater catalytic role compared to H$_2$O in

227 lowering the energy barrier for the hydrolysis of HNSO$_2$. In particular, MSA facilitates hydrogen

228 atom to extraction from H$_2$O, further reducing the reaction energy barriers to 7.7 kcal·mol^{-1}.

229 Meanwhile, the calculated rate coefficients for HNSO$_2$ hydrolysis with MSA was 3.08×10^{-11}-3.50

230 $\times 10^{-11}$ cm^3·molecule^{-1}·s^{-1} within 212.6-320.0 K, exceeding corresponding values for reactions

231 involving H$_2$O by 2 orders of magnitude. Besides, the Gibbs free energy of IMF_MSA1 was 2.0

232 kcal·mol^{-1} lower than that of the product complex IMF_WM1 (SFA···H$_2$O), suggesting SFA has a

233 higher affinity for MSA compared to H$_2$O. Besides, MSA-assisted HNSO$_2$ hydrolysis is reduced by

234 4.9 kcal·mol^{-1} in energy barrier than the NH$_3$-assisted ammonolysis of SO$_3$ with its rate constant at

235 298 K (2.85×10^{-11} cm^3·molecule^{-1}·s^{-1}) close to the value of ammonolysis of SO$_3$ with NH$_3$ ($4.35 \times$

236 10^{-10} cm^3·molecule^{-1}·s^{-1}) (Li et al., 2018). However, due to the absence of the concentration of

237     $HNSO_2$, the competitiveness of these two reactions cannot be further confirmed.

238   To evaluate the comparative catalytic ability of X ($X = H_2O$ and MSA) in the atmosphere, the

239   effective rate coefficients (k') for X-assisted $HNSO_2$ hydrolysis were calculated in Table 1. Notably,

240   k' serves as a metric for gauging the comparative catalytic ability of a series of gaseous catalysts in

241   atmospheric reactions (Sarkar et al., 2017; Zhang et al., 2020; Zhang et al., 2019; Buszek et al.,

242   2012; Gonzalez et al., 2011; Parandaman et al., 2018; Anglada et al., 2013). When X was present,

243   the calculated k' was given by Eq. (3).

244 $$k'_X = k_X \times K_{eq}(X \cdots H_2O) \times [X] \tag{3}$$

245   In Eq. (3), k_X was the rate coefficient for X-assisted $HNSO_2$ hydrolysis (Table 1), while $K_{eq}(X \cdots H_2O)$

246   denotes the equilibrium coefficients of $X \cdots H_2O$ (Table S2). $[X]$ represents the avaiable

247   concentrations of H_2O (Anglada et al., 2013) and MSA (Shen et al., 2020). As indicated in Table 1,

248   at experimental concentrations ($[H_2O] = 5.16 \times 10^{16}$-$2.35 \times 10^{18}$ molecules·cm^{-3}) within 280.0-320.0

249   K (at 0 km), the computed k'_{WM} ranged from 5.99×10^{-18}-7.79×10^{-17} cm^3·molecule^{-1}·s^{-1}. This range

250   exceeded k'_{MSA} (4.60×10^{-21}-4.81×10^{-20} cm^3·molecule^{-1}·s^{-1}) by 2-4 orders of magnitude,

251   highlighting pronounced impact of H_2O compared to MSA at 0 km in enhancing the rate of $HNSO_2$

252   hydrolysis. However, with the significant decrease in atmospheric water molecules with increasing

253   altitude, the calculated k'_{MSA} ranged from 1.96×10^{-19}·s^{-1}-1.30×10^{-17}·cm^3·molecule^{-1}·s^{-1},

254   surpassing k'_{WM} (9.85×10^{-27}-6.51×10^{-22}·cm^3·molecule^{-1}·s^{-1}) by 3-10 orders of magnitude. This

255   illustrates that MSA has a significantly greater catalytic ability than H_2O in accelerating the rate of

256     $HNSO_2$ hydrolysis within 5-15 km. So, $HNSO_2$ hydrolysis with MSA may represent a potential

257   formation pathway for SFA across an altitude scope of 5-15 km.

258 **3.2 Reactions at the air-water interface**

259   The interfacial mechanism of MSA-assisted $HNSO_2$ hydrolysis at the air-water interface has

260   not been thoroughly investigated. Interestingly, our simulations show that $HNSO_2$ and MSA

261   molecules spend approximately 49.1% and 12.1% of the time, respectively, at the air-water interface

262   during the 150 ns simulation (Fig. S1 and Fig. S6). This reveals that the presence of $HNSO_2$ and

263   MSA at the air-water interface should not be disregarded. Therefore, BOMD simulations were

264   performed to clarify the interfacial mechanism of MSA-assisted $HNSO_2$ hydrolysis at the air-water

265   interface. Comparable to the reactions of SO_3 at the air-water interface with acidic molecules (Cheng

266   et al., 2023; Zhong et al., 2019a), the hydrolysis of $HNSO_2$ with MSA at the air-water interface may

267   occur through three pathways: (*i*) the adsorbed MSA interacts with $HNSO_2$ at the air-water interface;

268   (*ii*) the adsorbed $HNSO_2$ interacts with MSA at the air-water interface; and (*iii*) the $HNSO_2 \cdots MSA$

269   complex reacts at the air-water interface. Nevertheless, because of the high reactiveness of MSA at

270   the air-water interface, the lifetime of MSA was minimal (seen in Fig. S9) on the water droplet,

271   which was around a small number of picoseconds leading to the rapid formation of MSA^- ion.

272   Meanwhile, although $HNSO_2$ remains stable at the air-water interface (seen in Fig. S8) and does not

273   dissociate within 10 ps, the hydrated form of $HNSO_2$ illustrated in Fig. S8 was not conducive to

274    $HNSO_2$ hydrolysis at the air-water interface. So, model (*iii*) was primarily considered for $HNSO_2$

275   hydrolysis with MSA at the air-water interface. It was worth noting that $HNSO_2 \cdots MSA$ complex

276   can persist at the air-water interface for approximately 34.2% of the 150 ns simulation time (see in

277   Fig. S7). For model (*iii*), two types of reactions were found at the air-water interface: (*a*) the

278    $NH_2SO_3^-$ and H_3O^+ ions formation mechanism, and (*b*) the proton exchange mechanism.

279   **$NH_2SO_3^-$ and H_3O^+ ions forming mechanism.** Fig. 2(a), Fig. S10 and Movie 1 illustrates the

280   formation mechanism of $NH_2SO_3^-$ and H_3O^+ ions through the chain structure. At 4.57 ps, a chain

281   hydrolyzed transition state was observed, accompanied by two protons transfer events. Specially,

282   an H2 atom transferred from the OH moiety of MSA molecule to the terminal N atom of $HNSO_2$

283   molecule, resulting in the breaking of the O3-H2 bond (with the length of 1.49 Å) and forming the

284   H2-N bond (with the length of 1.14 Å). Concurrently, an interfacial water molecule decomposes,

285   leading to the elongation of the O1-H1 bond to over 1.00 Å, with the S1 atom of $HNSO_2$ obtaining

286   the OH moiety of the interfacial water molecule ($d_{(S1-O1)}$ = 1.60 Å). By 4.61 ps, The N-H2 and S1-

287   O1 bonds both shortened to 0.99 Å and 1.01 Å, revealing the formation of the SFA molecule.

288   However, due to its strong acidity, the SFA molecule could only persist on the water droplet surface

289   for a ps time-scale. As a result, at 7.43 ps, the proton of SFA transferred to another interfacial water

290   molecule, completing the deprotonation of SFA. The loop structure mechanism (Fig. 2(b), Fig. S11

291   and Movie 2) was similar with the chain structure mechanism. However, in this case, the proton of

292   SFA transferred to $CH_3SO_3^-$ rather than to an interfacial water molecule.

293   **Proton exchange mechanism**. As depicted in Fig. 3, the proton exchange mechanism

294   illustrates the deprotonation of MSA concurrent with $HNSO_2$ hydration at the air-water interface.

295   As shown in Fig. 3(a), Fig. S12 and Movie 3, MSA-mediated hydration $HNSO_2$ with a single water

296   molecule was observed. Initially, the $HNSO_2 \cdots MSA$ complex quickly associates with an interfacial

297　water molecule, and forms a loop structure complex that accelerates the rate of proton transfer. By

298　4.38 ps, an eight-membered loop structure complex, $HNSO_2 \cdots H_2O \cdots MSA$, emerges, characterized

299　by two hydrogen bonds ($d_{(H2-N)}$ = 1.82 Å and $d_{(H1-O2)}$ = 1.92 Å) and a van der Waals forces ($d_{(S1-O1)}$

300　= 2.35 Å). Thereafter, at 4.77 ps, a transition state-like configuration was identified where the water

301　molecule within the loop complex dissociated, elongating the O1-H1 bond to over 1.00 Å, and the

302　S atom of $HNSO_2$ attaches to the OH group of the interfacial water molecule. Concurrently, the

303　$CH_3SO_3^-$ ion receives the proton from the separated interfacial water molecule. The entire reaction

304　for MSA-mediated hydration $HNSO_2$ with one water molecule was completed at 4.80 ps, resulting

305　in the formation of SFA and MSA molecules. MSA-mediated hydration of $HNSO_2$ with two water

306　molecules (Fig. 3(b), Fig. S13 and Movie 4) at the air-water interface was similar with mechanism

307　identified with one water molecule. However, the inclusion of two water molecules enlarges the

308　loop, significantly reducing the stress on the loop structures. Consistent with the prediction in Fig.

309　4, the loop structures preferred to include two water molecules rather than one water molecule. This

310　observation agrees well with the reported hydration of Criegee intermediate at the air-water interface

311　(Zhu et al., 2016; Kumar et al., 2018; Liu et al., 2021; Zhang et al., 2023a). Additionally, MSA-

312　mediated hydration of $HNSO_2$ with three water molecules (Fig. S14 and Movie 5) has been observed

313　in the proton exchange mechanism. However, its probability of occurrence was smaller due to the

314　relatively larger entropy effect. It was noteworthy that the SFA and MSA molecules formed in the

315　proton exchange mechanism were not stable at the air-water interface, which can further interact

316　with an interfacial water molecule to form the corresponding ions of $NH_2SO_3^-$ and $CH_3SO_3^-$.

317　　　At the air-water interface, a sum of 50 BOMD trajectories, each lasting 10 ps, were conducted

318　to investigate $HNSO_2$ hydrolysis with MSA. Two distinct mechanisms were observed: the formation

319　of $NH_2SO_3^-$ and H_3O^+ ions formation (shown in blue and yellow in Fig. 4) and the proton exchange

320　mechanism (represented by orange, purple and green in Fig. 4). In the mechanism involving the

321　formation of $NH_2SO_3^-$ and H_3O^+ ions, approximately 22% (Fig. 2(a), Fig. 4, Fig. S10 and Movie 1)

322　of the reactions took place via a chain structure, while the majority (~18%) (Fig. 2(b), Fig. 4, Fig.

323　S11 and Movie 2) proceeded through a loop structure mechanism. This discrepancy can be attributed

324　to the uncertainty regarding the direction of proton transfer from SFA. Since the number of water

325　molecules near the water microdroplet far exceeded that of $CH_3SO_3^-$, protons were predominantly

326　transferred to interface water molecules, making the loop structure mechanism weaker than the

327   chain structure mechanism. Approximately 60% of the reactions were observed to be due to the

328   proton exchange mechanism in BOMD simulations. Through water-mediated mechanisms, these

329   reactions resulted in SFA formation. Similarly to gas-phase reactions, loop structures were observed

330   in these reactions. Approximately 10% of the reactions formed a loop structure involving one water

331   molecule (Fig. 3(a), Fig. 4, Fig. S12 and Movie 3), while the most common loop structure involved

332   two water molecules (about 42%) (Fig. 3(b), Fig. 4, Fig. S13 and Movie 4). Smaller loops were

333   found to experience more stress than loop structures with two water molecules. In cases of loop

334   structures with three water molecules (about 8%) (Fig. 4, Fig. S14 and Movie 5), the entropy effect

335   was deemed to be more significant than the strain effect and likely played a dominant role. The two

336   water molecules contained in the loop structure not only acted as a reactant but also facilitated proton

337   transfer as a bridge.

338   **3.3 New Particle Formation from the atmospheric products**

339   **3.3.1. The influence of SFA on the stability of atmospheric MSA-MA-based**
340   **clusters**

341   Electrostatic Potential (ESP) mapping on the molecular van der Waals (vdW) surface was

342   employed to analyze the interactions between SFA and other key nucleation precursors like MSA

343   and MA. As shown in Fig. 5, sites with more negative ESP often attract more positive ESP sites,

344   namely hydrogen bonds in the studied system. Specifically, the hydrogen atoms of the $-SO_3H$ and -

345   NH_2 groups (site 4 and 5) in SFA, possessing more positive ESP values, have the potential to attract

346   groups with negative ESP values, such as the oxygen atom within the $-SO_3H$ group of MSA (site 6)

347   and the nitrogen atom of MA (site 1), thus forming hydrogen bonds as proton donors. Additionally,

348   the sulfur atom of the $-SO_3H$ functional group (site 7) in SFA, with a negative ESP of -30.75, acts

349   as proton acceptor, facilitating direct binding with MSA and MA molecules via the hydrogen bonds.

350   Therefore, the introduction of SFA was believed to enhance the stability of MSA-MA clusters by

351   promoting the formation of more hydrogen bonds and facilitating proton transfers.

352   **3.3.2. The cluster formation rates in the SFA-MSA-MA system**

353   Simulations were conducted to determine the cluster formation rates (J) for the MSA-MA-SFA

354   system, varying parameters such as temperature and the concentrations of the precursors were

355   involved. To assess the promotional impact of SFA on J under varying atmospheric conditions, the

356   enhancement factor (R) was computed as the ratio of $J_{MSA-MA-SFA}$ to J_{MSA-MA}. As depicted in Fig. 6

357 (a), the *J* of MSA-MA-SFA system exhibits a negative correlation with temperature, attributed to

358 the decrease in ΔG value and evaporation rates of clusters at lower temperatures. Conversely, a

359 positive correlation of *R* with temperature was observed (Fig. 6(b)), indicating that SFA's

360 enhancement of nucleation was more pronounced in regions with relatively higher temperatures.

361 Furthermore, both *J* and *R* show an increase as the [SFA] increases, suggesting a positive correlation

362 of *J* and *R* with [SFA]. In short, in regions with high [SFA], such as the Yangtze River Delta of

363 China, Bangladesh, and the east coast of India, SFA was expected to significantly boost the *J* of

364 MSA-MA based nucleation. It is noted that in Fig. 6(b), due to the competitive relationship between

365 MSA and SFA, at low concentrations of SFA, the binding capacity of MSA with MA is stronger

366 than that of SFA with MA, resulting in only a small amount of SFA participating in cluster formation.

367 However, as the concentration of SFA increases, the number of $(MSA)_x \cdot (MA)_y \cdot (SFA)_z$ (where $y \leq$

368 $x + z \leq 3$) ternary clusters increase, leading to the formation of more hydrogen bonds and a

369 significant increase in R_{SFA}. Additionally, Fig. 7 illustrates the *J* and *R* of MSA-MA-SFA clusters

370 under different [MSA] and [MA]. On one hand, larger values of [MSA] and [MA] correspond to

371 higher *J*, as the increased concentration of nucleation precursors leads to a rise in the number of

372 MSA-MA-FSA clusters. On the other hand, increasing [MSA] and [MA] result in a decrease in the

373 *R* attributed to the effect of SFA on nucleation. This was because as [MSA] and [MA] increases,

374 the prevalence of pure MSA-MA clusters rise during the clustering process, consequently reducing

375 the impact of SFA.

3.3.3. The growth paths of cluster under different atmospheric conditions

377 Li et al. studied the atmospheric concentration of SFA estimated by theoretical method (Li et

378 al., 2018) was expected to reach up to10^8 molecules·cm^{-3} in high NH_3 concentrations, such as

379 Yangtze River Delta in China (Yu et al., 2020), Indo-Gangetic Plains (Kuttippurath et al., 2020),

380 Pakistan, Bangla desh (Warner et al., 2016), and the southern Italy (Tang et al., 2021). Considering

381 the high-atmospheric concentrations of MSA and MA detected in coastal industrial areas (Stieger

382 et al., 2021; Mochizuki et al., 2017;), SFA could be an important contributor to MSA-MA-driven

383 NPF, such as the Yangtze River Delta in China, the east coast of India, the south of Bangladesh and

384 Italy. To further evaluate the implication of SFA for the MSA-MA nucleation in the atmosphere,

385 the growth paths of cluster was calculated under different atmospheric conditions. In Fig. 8 (a), two

386 main types of cluster formation routes were found: (*i*) the pure MSA-MA pathway and (*ii*) the MSA-

387   MA-SFA pathways at 278.15 K in the studied system. In the pure MSA-MA pathway, cluster

388   growth primarily occurs through the collisional addition of MSA or MA monomers. Conversely, in

389   the SFA-involved pathways, SFA can directly participate in the formation of stable larger clusters

390   subsequently, such as $(MSA)_2 \cdot (MA)_2 \cdot SFA$ and $(MSA)_2 \cdot (MA)_2 \cdot (SFA)_2$ clusters, and then

391   subsequently grow out. The involvement of SFA in the cluster formation pathway was significantly

392   influenced by atmospheric conditions. Firstly, as the temperature rises from 238.15 K to 278.15 K,

393   the contribution of the SFA-involved cluster formation pathways rises from 68% to 90% (Fig. 8

394   (b)), implying that the pathway involving SFA becomes increasingly important at lower altitudes or

395   in warmer conditions. Secondly, as depicted in Fig. 8(c) and Fig. S22, the contribution of SFA to

396   the MSA-MA system is primarily influenced by [SFA] and [MSA], with negligible dependence on

397   [MA]. To assess the role of SFA in MSA-MA nucleation in the atmosphere, the specific contribution

398   of the MSA-MA cluster growth paths at varying [SFA] to NPF was calculated at 278.15 K, as

399   illustrated in Fig. 8(c), under the ambient conditions typical of the corresponding regions. Generally,

400   as [SFA] increases from 10^4 to 10^8 molecules$\cdot$cm^{-3}, the contribution of the SFA-involved pathway

401   increases gradually. Specifically, at low [SFA] (10^4 molecules$\cdot$cm^{-3}), the contributions of SFA-

402   involved clustering pathways are 77% and 41% in regions with relatively low [MSA] in non-sea

403   regions (Berresheim et al., 2002). In regions with high [SFA] (10^6, 10^8 molecules$\cdot$cm^{-3}), the

404   contributions of the SFA-MSA-MA growth pathways are dominant in their NPF. Particularly in

405   areas with high [MSA], such as the Pacific Rim (6.26×10^8 molecules$\cdot$cm^{-3} (Saltzman et al., 1986)),

406   the central Mediterranean Sea (2.11×10^8 molecules$\cdot$cm^{-3} (Mansour et al., 2020)) and the Amundsen

407   Sea (3.65×10^9 molecules$\cdot$cm^{-3} (Jung et al., 2020)), nucleation is primarily driven by the SFA-

408   MSA-MA pathway, contributing to approximately 88% of cluster formation. These results suggest

409   that the influence of SFA is more pronounced in regions with relatively high [MSA]. It is important

410   to note that the [SFA] values discussed in this work are estimated from limited observational data

411   based on the reaction between SO_3 and NH_3 in the atmosphere. Accurate determination of

412   atmospheric [SFA] requires extensive field observations to enable more comprehensive research.

413   **3.4 Interfacial implications of products on aerosol particle growth**

414   As the discussion above, the formation of $SFA^- \cdots H_3O^+$ and $MSA^- \cdots H_3O^+$ ions pairs can occur

415   within a few picoseconds at the air-water interface. The atmospheric affinity of MSA^-, SFA^- and

416   H_3O^+ for gaseous precursors was further probed by evaluating the free energies of interaction. It

was worth noting that compounds such as MSA, MA, HNO$_3$ (NA), and (COOH)$_2$ (OA) were identified as candidate species for consideration (Wang et al., 2024; Kulmala et al., 2004). As presented in Table 2, the computed binding energies demonstrate that the interactions of SFA$^-$···MSA, SFA$^-$···NA, SFA$^-$···OA, H$_3$O$^+$···MA, MSA$^-$···MSA, MSA$^-$···OA, and MSA$^-$···NA were stronger than those of MSA···MA (one of the primary precursors for atmospheric aerosols), with their Gibbs free energies increased by 14.3-50.9 kcal·mol^{-1}. The findings indicate that the presence of SFA$^-$, MSA$^-$, and H$_3$O$^+$ at the interface facilitates the capture of potential gaseous species onto the surface of water microdroplet.

Furthermore, we investigated the possibility of SFA$^-$ contributing to the enlargement of particles within the MSA-MA cluster, taking into account the geometric configuration and the free energy of formation for the (MSA)$_1$·(MA)$_1$·(SFA$^-$)$_1$ clusters aggregating. Compared with other clusters, such as (MSA)$_1$·(MA)$_1$·(X)$_1$ (where X = HCOOH, CH$_3$COOH, CHOCOOH, OA, CH$_3$COCOOH, HOOCCH$_2$COOH, HOOC(CH)$_2$COOH, HOOC(CH$_2$)$_2$COOH, HOOC(CH$_2$)$_3$COOH, C$_6$H$_5$(COOH) and C$_{10}$H$_{16}$O$_3$) clusters (Zhang et al, 2022), the quantity of hydrogen bonds within the (MSA)$_1$·(MA)$_1$·(SFA$^-$)$_1$ cluster has increased, and the loop of complex was expanded. It has been demonstrated that SFA$^-$ has the greatest capacity to stabilize MSA-MA clusters and facilitate MSA-MA nucleation in these clusters. This was attributed to its acidic nature and structural characteristics, which include a greater number of intermolecular hydrogen bond binding sites. Therefore, relative to (MSA)$_1$·(MA)$_1$·(X)$_1$ cluster (Table 2), the Gibbs formation free energy ΔG of the (MSA)$_1$·(MA)$_1$·(SFA$^-$)$_1$ cluster was lower, indicating that the NH$_2$SO$_3^-$ ion exhibits a more potent nucleation capacity at the air-water interface compared to the X species in the gas phase. Consequently, our forecast was that the presence of NH$_2$SO$_3^-$ at the air-water interface will foster enhanced particle growth.

4. Summary and Conclusions

In this study, quantum chemical calculations, BOMD simulations and ACDC kinetic model were utilized to characterize the gaseous and interfacial hydrolysis of HNSO$_2$ with MSA, and to examine the influence exerted by SFA on MSA-MA-based clusters.

In the gaseous reaction, the activation energy for the hydrolysis of HNSO$_2$ catalyzed by MSA was only 0.8 kcal·mol^{-1}, significantly lower by 7.7 kcal·mol^{-1} than the energy barrier of H$_2$O-assisted

446 HNSO$_2$ hydrolysis. The effective rate coefficients reveal that the SFA formation from MSA-

447 catalyzed hydrolysis of HNSO$_2$ can be competitive with that catalyzed by H$_2$O within an altitude of

448 5-15 km. Moreover, kinetic simulations utilizing the ACDC have disclosed that SFA has an

449 unexpectedly positive impact on the NPF process, markedly enhancing the assembly of MSA-MA-

450 based cluster. Notably, the "participant" mechanism of SFA for cluster formation has been identified

451 by tracing the growth paths of the system in agriculture-developed and coastal industrial areas,

452 especially significant in the Yangtze River Delta of China, Bangladesh, and the east coast of India.

453   At the air-water interface, the NH$_2$SO$_3^-$ and H$_3$O$^+$ ions forming mechanism (~40%) and the

454 proton exchange mechanism (~60%) were observed in the hydrolysis of HNSO$_2$ with MSA, which

455 can take place in a few picoseconds. Notably, the formed SFA$^-$, MSA$^-$, and H$_3$O$^+$ ions at the air-

456 water interface possess the ability to attract potential precursor molecules like MSA, MA, and

457 HNO$_3$. This attraction facilitates the transition of gaseous molecules onto the surface of water

458 microdroplet. Moreover, the assessment of the potential of X in the formation of the ternary MSA-

459 MA-X cluster revealed that SFA$^-$ exhibits the greatest propensity to stabilize MSA-MA clusters and

460 to foster nucleation of MSA-MA in the context of X.

461   Overall, this work not only elucidates a novel mechanism underlying the hydrolysis of HNSO$_2$

462 with MSA, but also highlight the potential contribution of SFA on aerosol particle growth and new

463 particle formation.

464 **Acknowledgments**

468 **Declaration of competing interest**

469   The authors declare that they have no known competing financial interests or personal

470 relationships that could have appeared to influence the work reported in this paper.

Reference

Adler, T. B., Knizia, G., and Werner, H. J.: A simple and efficient CCSD(T)-F12 approximation, J. Chem. Phys., 127, 22, 2007.

Anglada, J. M., Hoffman, G. J., Slipchenko, L. V. M., Costa, M., Ruiz-Lopez, M. F., and Francisco, J. S.: Atmospheric significance of water clusters and ozone-water complexes, J. Phys. Chem. A, 117, 10381-10396, 2013.

Bao, J. L., Zhang, X., and Truhlar, D. G.: Barrierless association of CF_2 and dissociation of C_2F_4 by variational transition-state theory and system-specific quantum Rice-Ramsperger-Kassel theory, Proc. Natl. Acad. Sci. USA., 113, 13606-13611, 2016.

Becke, A. D.: Density-functional exchange-energy approximation with correct asymptotic behavior, Phys. Rev. A., 38, 3098-3100, 1988.

Berresheim, H., Elste, T., Tremmel, H. G., Allen, A. G., Hansson, H. C., Rosman, K., Dal Maso, M., Mäkelä, J. M., Kulmala, M., and O'Dowd, C. D.: Gas-aerosol relationships of H_2SO_4, MSA, and OH: Observations in the coastal marine boundary layer at Mace Head, Ireland, J. Geophys. Res. Atmos., 107, PAR 5-1-PAR 5-12, 2002.

Bork, N., Elm, J., Olenius, T., and Vehkamäki, H.: Methane sulfonic acid-enhanced formation of molecular clusters of sulfuric acid and dimethyl amine, Atmos. Chem. Phys., 14, 12023-12030, 2014.

Bork, N., Du, L., Reiman, H., Kurten, T., and Kjaergaard, H. G.: Benchmarking ab initio binding energies of hydrogen-bonded molecular clusters based on FTIR spectroscopy, J. Phys. Chem. A, 118, 5316-5322, 2014.

Buszek, R. J., Torrent-Sucarrat, M., Anglada, J. M., and Francisco, J. S.: Effects of a single water molecule on the OH + H_2O_2 reaction, J. Phys. Chem. A, 116, 5821-5829, 2012.

Chen, D., Li, D., Wang, C., Luo, Y., Liu, F., and Wang, W.: Atmospheric implications of hydration on the formation of methanesulfonic acid and methylamine clusters: A theoretical study, Chemosphere., 244, 125538-125547, 2020.

Chen, H. and Finlayson-Pitts, B. J.: New particle formation from methanesulfonic acid and amines/ammonia as a function of temperature, Environ. Sci. Technol., 51, 243-252, 2017.

Chen, H., Varner, M. E., Gerber., R. B., Finlayson-Pitts, B. J., Reactions of methanesulfonic acid with amines and ammonia as a source of new particles in air. J. Phys. Chem. B 2016, 120, 1526-1536.

Cheng, Y., Ding, C., Wang, H., Zhang, T., Wang, R., Muthiah, B., Xu, H., Zhang, Q., and Jiang, M.: Significant influence of water molecules on the SO_3 + HCl reaction in the gas phase and at the air-water interface, Phys. Chem. Chem. Phys., 25, 28885-28894, 2023.

Chuang, Y., Corchado, J., Fast, P., Villa, J., Coitino, E., Hu, W., Liu, Y., Lynch, G., Nguyen, K., and Jackels, C.: Polyrate-version 8.2, University of Minnesota, Minneapolis, 1999.

Dawson, M. L., Varner, M. E., Perraud, V., Ezell, M. J., Gerber, R. B., and Finlayson-Pitts, B. J.: Simplified mechanism for new particle formation from methanesulfonic acid, amines, and water via experiments and ab initio calculations, Proc. Natl. Acad. Sci. USA., 109, 18719-18724, 2012.

Dawson, M. L., Varner, M. E., Perraud, V. M., Ezell, M. J., Wilson, J. M., Zelenyuk, A., Gerber, R. B., and Finlayson-Pitts, B. J.: Amine-amine exchange in aminium-methanesulfonate aerosols, J. Phys. Chem. C., 118(50):29431-29440, 2014.

Deng, G., Wu, Z., Li, D., Linguerri, R., Francisco, J. S., and Zeng, X. J. J. o. t. A. C. S.: Simplest N-Sulfonylamine $HNSO_2$, J. Am. Chem. Soc, 140, 138, 11509-11512, 2016.

Ding, C., Cheng, Y., Wang, H., Yang, J., Li, Z., Lily, M., Wang, R., and Zhang, T.: Determination of the

influence of water on the SO_3 + CH_3OH reaction in the gas phase and at the air-water interface, Phys. Chem. Chem. Phys., 25, 15693-15701, 2023.

Elm, J.: Clusteromics II: methanesulfonic acid-base cluster formation, ACS omega., 6, 17035-17044, 2021.

Elm, J., Bilde, M., and Mikkelsen, K. V.: Assessment of density functional theory in predicting structures and free energies of reaction of atmospheric prenucleation clusters, J. Chem. Theory Comput., 8, 2071-2077, 2012.

Freeling, F., Scheurer, M., Sandholzer, A., Armbruster, D., Nödler, K., Schulz, M., Ternes, T. A., and Wick, A.: Under the radar – Exceptionally high environmental concentrations of the high production volume chemical sulfamic acid in the urban water cycle, Water Research., 175, 115706, 2020.

Frisch, M. J., Trucks, G. W., Schlegel, H. B., Scuseria, G. E., Robb, M. A., Cheeseman, J. R., Scalmani, G., Barone, V., Mennucci, B., Petersson, G. A., Nakatsuji, H., Caricato, M., Li, X., Hratchian, H. P., Izmaylov, A. F., Bloino, J., Zheng, G., Sonnenberg, J. L., Hada, M., Ehara, M., Toyota, K., Fukuda, R., Hasegawa, J., Ishida, M., Nakajima, T., Honda, Y., Kitao, O., Nakai, H., Vreven, T., Montgomery, J. A. Jr., Peralta, J. E., Ogliaro, F., Bearpark, M., Heyd, J. J., Brothers, E., Kudin, K. N., Staroverov, V. N., Kobayashi, R., Normand, J., Raghavachari, K., Rendell, A., Burant, J. C., Iyengar, S. S., Tomasi, J., Cossi, M., Rega, N., Millam, J. M., Klene, M., Knox, J. E., Cross, J. B., Bakken, V., Adamo, C., Jaramillo, J., Gomperts, R., Stratmann, R. E., Yazyev, O., Austin, A. J., Cammi, R., Pomelli, C., Ochterski, J. W., Martin, R. L., Morokuma, K., Zakrzewski, V. G., Voth, G. A., Salvador, P., Dannenberg, J. J., Dapprich, S., Daniels, A. D., Farkas, Ö., Foresman, J. B., Ortiz, J. V., Cioslowski, J., and Fox, D. J: Gaussian09 Revision D. 01, Gaussian Inc. Wallingford CT, Gaussian Inc. Wallingford CT, See also: URL: http://www. gaussian. com, 2009.

Georgievskii, Y. and Klippenstein, S.: Variable reaction coordinate transition state theory: analytic results and application to the C_2H_3 + H → C_2H_4 reaction, JCP, 118, 5442-5455, 2003.

Glowacki, D. R., Liang, C.-H., Morley, C., Pilling, M. J., and Robertson, S. H.: MESMER: an open-source master equation solver for multi-energy well reactions, J. Phys. Chem. A, 116, 9545-9560, 2012.

Goedecker, S., Teter, M., and Hutter, J.: Separable dual-space Gaussian pseudopotentials, Phys. Rev. B., 54, 1703, 1996.

Gonzalez, J., Anglada, J. M., Buszek, R. J., and Francisco, J. S.: Impact of water on the OH + HOCl reaction, J. Am. Chem. Soc, 133, 3345-3353, 2011.

Grimme, S., Antony, J., Ehrlich, S., and Krieg, H.: A consistent and accurate ab initio parametrization of density functional dispersion correction (DFT-D) for the 94 elements H-Pu, J. Chem. Phys., 132, 154104, 2010.

Hartwigsen, C., Gœdecker, S., and Hutter, J.: Relativistic separable dual-space Gaussian pseudopotentials from H to Rn, Phys. Rev. B., 58, 3641-3662, 1998.

Hirota, K., Mäkelä, J., and Tokunaga, O.: Reactions of sulfur dioxide with ammonia: Dependence on oxygen and nitric oxide, Ind. Eng. Chem. Res., 35, 3362-3368, 1996.

Hu, Y., Chen, S., Ye, S., Wei, S., Chu, B., Wang, R., Li, H., and Zhang, T.: The role of trifluoroacetic acid in new particle formation from methanesulfonic acid-methylamine, Atmos. Environ., 311, 120001, 2023.

Hutter, J., Iannuzzi, M., Schiffmann, F., and VandeVondele, J.: Cp2k: atomistic simulations of condensed matter systems, WIRES COMPUT MOL SCI., 4, 15-25, 2014.

Jung, J., Hong, S. B., Chen, M., Hur, J., Jiao, L., Lee, Y., Park, K., Hahm, D., Choi, J. O., Yang, E. J., and Physics: Characteristics of methanesulfonic acid, non-sea-salt sulfate and organic carbon aerosols over the Amundsen Sea, Antarctica, Atmos. Chem. Phys., 20, 5405-5424, 2020.

Kendall, R. A., T. H. D., and Harrison, R. J.: Electron affinities of the first-row atoms revisited. Systematic basis sets and wave functions, J. Chem. Phys., 96, 6796-6806, 1992.

Kim, T. O., Ishida, T., Adachi, M., Okuyama, K., and Seinfeld, J. H.: Nanometer-sized particle formation from $NH_3/SO_2/H_2O$/air mixtures by ionizing irradiation, Aerosol Sci. Tech., 29, 111-125, 1998.

Kolb, C., Jayne, J., Worsnop, D., Molina, M., Meads, R., and Viggiano, A.: Gas phase reaction of sulfur trioxide with water vapor, J. Am. Chem. Soc., 116, 10314-10315, 1994.

Kulmala, M., Vehkamäki, H., Petäjä, T., Dal Maso, M., Lauri, A., Kerminen, V. M., Birmili, W., and McMurry, P. H.: Formation and growth rates of ultrafine atmospheric particles: a review of observations, J. Aerosol Sci., 35, 143-176, 2004.

Kumar, M., Li, H., Zhang, X., Zeng, X. C., and Francisco, J. S.: Nitric acid-amine chemistry in the gas phase and at the air-water interface, J. Am. Chem. Soc., 140, 6456-6466, 2018.

Kuttippurath, J., Singh, A., Dash, S., Mallick, N., Clerbaux, C., Van Damme, M., Clarisse, L., Coheur, P.-F., Raj, S., and Abbhishek, K.: Record high levels of atmospheric ammonia over India: Spatial and temporal analyses, Sci. Total Environ., 740, 139986, 2020.

Larson, L. J. and Tao, F.-M.: Interactions and reactions of sulfur trioxide, water, and ammonia: An ab initio and density functional theory study, J. Phys. Chem. A, 105, 4344-4350, 2001.

Lee, C., Yang, W., and Parr, R. G.: Development of the colle-Salvetti correlation-energy formula into a functional of the electron density, PHYS REV B, 37, 785, 1988.

Li, H., Zhong, J., Vehkamäki, H., Kurtén, T., Wang, W., Ge, M., Zhang, S., Li, Z., Zhang, X., Francisco, J. S., and Zeng, X. C.: Self-Catalytic reaction of SO_3 and NH_3 to produce sulfamic acid and its implication to atmospheric particle formation, J. Am. Chem. Soc, 140, 11020-11028, 2018.

Liu, J., Liu, Y., Yang, J., Zeng, X. C., and He, X.: Directional proton transfer in the reaction of the simplest criegee intermediate with water involving the formation of transient H_3O^+, J. Phys. Chem. Lett., 12, 3379-3386, https://doi.org/10.1021/acs.jpclett.1c00448, 2021.

Liu, L., Yu, F., Tu, K., Yang, Z., and Zhang, X.: Influence of atmospheric conditions on the role of trifluoroacetic acid in atmospheric sulfuric acid-dimethylamine nucleation, Atmos. Chem. Phys., 21, 6221-6230, 2021.

Long, B., Chang, C.-R., Long, Z.-W., Wang, Y.-B., Tan, X.-F., and Zhang, W.-J.: Nitric acid catalyzed hydrolysis of SO_3 in the formation of sulfuric acid: a theoretical study, Chem. Phys. Lett., 581, 26-29, 2013

Long, B., Wang, Y., Xia, Y., He, X., Bao, J. L., and Truhlar, D. G.: Atmospheric Kinetics: Bimolecular Reactions of Carbonyl Oxide by a Triple-Level Strategy, J. Am. Chem. Soc., 143, 8402-8413, 2021.

Long, B., Xia, Y., Zhang, Y.-Q., and Truhlar, D. G.: Kinetics of sulfur trioxide reaction with water vapor to form atmospheric sulfuric acid, J. Am. Chem. Soc., 145, 19866-19876, 2023.

Lovejoy, E. R. and Hanson, D. R.: Kinetics and products of the reaction $SO_3 + NH_3 + N_2$, J. Phys. Chem., 100, 4459-4465, 1996.

Ma, X., Zhao, X., Huang, Z., Wang, J., Lv, G., Xu, F., Zhang, Q., and Wang, W.: Determination of reactions between Criegee intermediates and methanesulfonic acid at the gas-liquid interface, Sci. Total Environ., 707, 135804, 2020.

Mai, T. V. T., Duong, M. V., Nguyen, H. T., and Huynh, L. K.: Ab initio kinetics of the $HOSO_2 + {}^3O_2 \rightarrow SO_3 + HO_2$ reaction, Phys. Chem. Chem. Phys., 20, 6677-6687, 2018.

Manonmani, G., Sandhiya, L., and Senthilkumar, K. J. I. J. O. Q. C.: Hydrolysis of $HNSO_2$: A potential route for atmospheric production of H_2SO_4 and NH_3, Int. J. Quantum Chem., 120, e26182, 2020.

Mansour, K., Decesari, S., Bellacicco, M., Marullo, S., Santoleri, R., Bonasoni, P., Facchini, M. C.,

Ovadnevaite, J., Ceburnis, D., and O'Dowd, C.: Particulate methanesulfonic acid over the central Mediterranean Sea: source region identification and relationship with phytoplankton activity, Atmos. Res., 237, 104837, 2020.

McGrath, M.J., Olenius, T., Ortega, I.K., Loukonen, V., Paasonen, P., Kurtén, T., Kulmala, M., Vehkamäki, H., Atmospheric cluster dynamics code: a flexible method for solution of the birth-death equations. Atmos. Chem. Phys. 12, 2345-2355, 2012.

Meana-Pañeda, R., Zheng, J., Bao, J. L., Zhang, S., Lynch, B. J., Corchado, J. C., Chuang, Y.-Y., Fast, P. L., Hu, W.-P., and Liu, Y.-P.: Polyrate 2023: A computer program for the calculation of chemical reaction rates for polyatomics. New version announcement, Comput Phys Commun, 294, 108933, 2024.

Neese, F.: The ORCA program system, WIREs Comput. Mol. Sci., 2, 73-78, 2012.

Parandaman, A., Perez, J. E., and Sinha, A.: Atmospheric decomposition of trifluoromethanol catalyzed by formic acid, J. Phys. Chem. A, 122, 9553-9562, 2018.

Pszona, M., Haupa, K., Bil, A., Mierzwicki, K., Szewczuk, Z., and Mielke, Z.: Clustering of sulfamic acid: ESI MS and theoretical study, J. Mass Spectrom., 50, 127-135, 2015.

Rennebaum, T., van Gerven, D., Sebastian, S. S., and Wickleder, M. S.: Hydrazine sulfonic acid, $NH_3NH(SO_3)$, the bigger sibling of sulfamic acid, CHEM-EUR J, 30, e202302526, 2024.

Saltzman, E., Savoie, D., Prospero, J., and Zika, R.: Methanesulfonic acid and non-sea-salt sulfate in Pacific air: Regional and seasonal variations, J. Atmos. Chem., 4, 227-240, 1986.

Sarkar, S., Mallick, S., Kumar, P., and Bandyopadhyay, B.: Isomerization of methoxy radical in the troposphere: Competition between acidic, neutral and basic catalysts, Phys. Chem. Chem. Phys., 19, 27848-27858, 2017.

Shang, D., Tang, L., Fang, X., Wang, L., Yang, S., Wu, Z., Chen, S., Li, X., Zeng, L., Guo, S., and Hu, M.: Variations in source contributions of particle number concentration under long-term emission control in winter of urban Beijing, Environ. Pollut., 304, 119072, 2022.

Shen, J., Elm, J., Xie, H.-B., Chen, J., Niu, J., and Vehkamaki, H.: Structural effects of amines in enhancing methanesulfonic acid-driven new particle formation, Environ. Sci. Technol., 54, 13498-13508, 2020.

Shen, J., Xie, H.-B., Elm, J., Ma, F., Chen, J., and Vehkamaki, H.: Methanesulfonic acid-driven new particle formation enhanced by monoethanolamine: A computational study, Environ. Sci. Technol., 53, 14387-14397, 2019.

Chen, H.; Varner, M. E.; Gerber, R. B.; Finlayson-Pitts, B. J.: Reactions of methanesulfonic acid with amines and ammonia as a source of new particles in air, J. Phys. Chem. B, 120, 1526-1536, 2016.

Shi, Z., Ford, J., and Castleman Jr, A.: Cluster reactions of surlfur trioxide and ammonia, Chemical physics letters, 220, 274-280, 1994.

Tang, Y. S., Flechard, C. R., Dämmgen, U., Vidic, S., Djuricic, V., Mitosinkova, M., Uggerud, H. T., Sanz, M. J., Simmons, I., and Dragosits, U.: Pan-European rural monitoring network shows dominance of NH_3 gas and NH_4NO_3 aerosol in inorganic atmospheric pollution load, Atmos. Chem. Phys., 21, 875-914, 2021.

Tsona Tchinda, N., Du, L., Liu, L., and Zhang, X.: Pyruvic acid, an efficient catalyst in SO_3 hydrolysis and effective clustering agent in sulfuric-acid-based new particle formation, Atmos. Chem. Phys., 22, 1951-1963, 2022.

Van Stempvoort, D., Spoelstra, J., Brown, S., Robertson, W., Post, R., and Smyth, S.: Sulfamate in environmental waters, Sci. Total Environ., 695, 133734, 2019.

VandeVondele, J. and Hutter, J.: Gaussian basis sets for accurate calculations on molecular systems in

gas and condensed phases, J. Chem. Phys., 127, 114105, 2007.

VandeVondele, J., Krack, M., Mohamed, F., Parrinello, M., Chassaing, T., and Hutter, J.: Quickstep: Fast and accurate density functional calculations using a mixed Gaussian and plane waves approach, Comput. Phys. Commun., 167, 103-128, 2005.

Wang, R., Cheng, Y., Chen, S., Li, R., Hu, Y., Guo, X., Zhang, T., Song, F., and Li, H.: Reaction of SO_3 with H_2SO_4 and its implications for aerosol particle formation in the gas phase and at the air-water interface, Atmos. Chem. Phys., 24, 4029-4046, 2024.

Wang, S., Nan, J., Shi, C., Fu, Q., Gao, S., Wang, D., Cui, H., Saiz-Lopez, A., and Zhou, B.: Atmospheric ammonia and its impacts on regional air quality over the megacity of Shanghai, China, Sci. Rep, 5, 15842, 2015.

Warner, J. X., Wei, Z., Strow, L. L., Dickerson, R. R., Nowak, J. B., and Physics: The global tropospheric ammonia distribution as seen in the 13-year AIRS measurement record, Atmos. Chem. Phys., 16, 5467-5479, 2016.

Xue, J., Shao, X., Li, J., Li, J., Trabelsi, T., Francisco, J. S., and Zeng, X.: Observation of the Water-$HNSO_2$ complex, J. Am. Chem. Soc., 146, 5455-5460, 2024.

Yu, X., Shen, L., Hou, X., Yuan, L., Pan, Y., An, J., and Yan, S.: High-resolution anthropogenic ammonia emission inventory for the Yangtze River Delta, China, CHEMOSPHERE, 251, 126342, 2020.

Zhang, J. and Dolg, M.: AB Cluster: the artificial bee colony algorithm for cluster global optimization, Phys. Chem. Chem. Phys., 17, 24173-24181, 2015.

Zhang, R., Khalizov, A., Wang, L., Hu, M., and Xu, W.: Nucleation and growth of nanoparticles in the atmosphere, Chem. Rev., 112, 1957-2011, 2012.

Zhang, R., Shen, J., Xie, H. B., Chen, J., and Elm, J.: The role of organic acids in new particle formation from methanesulfonic acid and methylamine, Atmos. Chem. Phys., 22, 2639-2650, 2022.

Zhang, T., Wen, M., Cao, X., Zhang, Y., Zeng, Z., Guo, X., Zhao, C., Lily, M., and Wang, R.: The hydrolysis of NO_2 dimer in small clusters of sulfuric acid: A potential source of nitrous acid in troposphere, Atmos. Environ., 243, 117876, 2020.

Zhang, T., Wen, M., Ding, C., Zhang, Y., Ma, X., Wang, Z., Lily, M., Liu, J., and Wang, R.: Multiple evaluations of atmospheric behavior between Criegee intermediates and HCHO: Gas-phase and gas-liquid interface reaction, J. Environ. Sci., 127, 308-319, 2023.

Zhang, T., Wen, M., Zhang, Y., Lan, X., Long, B., Wang, R., Yu, X., Zhao, C., and Wang, W.: Atmospheric chemistry of the self-reaction of HO_2 radicals: stepwise mechanism versus one-step process in the presence of $(H_2O)_n$ ($n = 1$-3) clusters, Phys. Chem. Chem. Phys., 21, 24042-24053, 2019.

Zhang, T., Zhang, Y., Tian, S., Zhou, M., Liu, D., Lin, L., Zhang, Q., Wang, R., and Muthiah, B.: Possible atmospheric source of NH_2SO_3H: the hydrolysis of $HNSO_2$ in the presence of neutral, basic, and acidic catalysts, Phys. Chem. Chem. Phys., 24, 4966-4977, 2022.

Zhang, X., Lian, Y., Tan, S., Yin, S., and Physics: Organ sulfate produced from consumption of SO_3 speeds up sulfuric acid-dimethylamine atmospheric nucleation, Atmos. Chem. Phys., 24, 3593-3612, 2024.

Zhang, Y., Wang, Z., Wang, H., Cheng, Y., Zhang, T., Ou, T., and Wang, R.: Atmospheric chemistry of NH_2SO_3H in polluted areas: an unexpected isomerization of NH_2SO_3H in acid-polluted regions, J. Phys. Chem. A, 127, 8935-8942, 2023.

Zhao, X., Shi, X., Ma, X., Zuo, C., Wang, H., Xu, F., Sun, Y., and Zhang, Q.: 2-Methyltetrol sulfate ester-initiated nucleation mechanism enhanced by common nucleation precursors: A theory study, Sci. Total Environ., 723, 137987, 2020.

690 Zhao, Y. and Truhlar, D. G.: The M06 suite of density functionals for main group thermochemistry,
691 thermochemical kinetics, noncovalent interactions, excited states, and transition elements: two new
692 functionals and systematic testing of four M06-class functionals and 12 other functionals, Theor. Chem.
693 Acc., 120, 215-241, 2008.
694 Zhong, J., Kumar, M., Francisco, J. S., and Zeng, X. C.: Insight into chemistry on cloud/aerosol water
695 surfaces, Acc. Chem. Res., 51, 1229-1237, 2018.
696 Zhong, J., Kumar, M., Zhu, C. Q., Francisco, J. S., and Zeng, X. C.: Frontispiece: surprising stability of
697 larger criegee intermediates on aqueous interfaces, ANGEW CHEM INT EDIT, 56, 7740-7744, 2017.
698 Zhong, J., Li, H., Kumar, M., Liu, J., Liu, L., Zhang, X., Zeng, X. C., and Francisco, J. S.: Mechanistic
699 insight into the reaction of organic acids with SO_3 at the air-water interface, ANGEW CHEM INT EDIT.,
700 131, 8351-8355, 2019.
701 Zhu, C., Kumar, M., Zhong, J., Li, L., Francisco, J. S., and Zeng, X. C.: New mechanistic pathways for
702 Criegee-water chemistry at the air/water interface, J. Am. Chem. Soc., 138, 11164-11169, 2016.
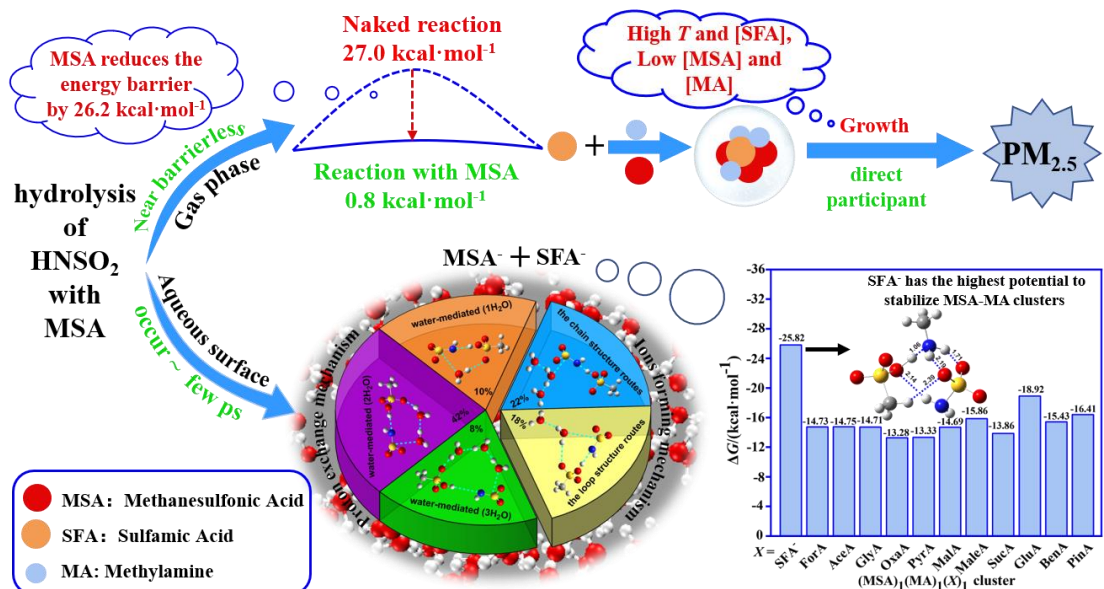
Graphical abstract

Figure Captions

706 **Fig. 1** The potential energy profile (ΔG) for the hydrolysis reaction of $HNSO_2$ with MSA at the

707 CCSD(T)-F12/cc-pVDZ-F12//M06-2X/6-311++G(2df,2pd) level of theory

708

709

710 **Fig. 2** BOMD simulation trajectories and snapshots of $NH_2SO_3^-$ and H_3O^+ ions forming mechanism

711 (chain structure (a) and loop-structure (b)) in the $HNSO_2$ hydrolysis with MSA at the air-water

712 interface

713

714

715 **Fig. 3** BOMD simulation trajectories and snapshots of proton exchange mechanism in MSA-

716 mediated hydration $HNSO_2$ with one (a) and two (b) water molecules at the air-water interface

717

718

719 **Fig. 4** Percentages of different mechanisms for the $HNSO_2$ hydrolysis with MSA at the air-water

720 interface observed in BOMD simulations

721

722

723 **Fig. 5** ESP-mapped molecular vdW surface of MA, SFA and MSA molecules at M06-2X/6-

724 311++G(2df,2pd) level of theory. Surface local minima and maxima of ESP of the different

725 functional groups in MA, SFA and MSA molecules are represented as blue and yellow spheres,

726 respectively. The values of maximum and minimum are shown in kcal mol^{-1} in the parentheses. The

727 green, red and blue arrows refer to the tendencies to form hydrogen bonds and proton transfer events,

728 respectively. (green = carbon, red = oxygen, blue = nitrogen, yellow = sulfur and white = hydrogen.)

729

730

731 **Fig. 6** The J (cm^{-3} s^{-1}) (a) and R (b) versus [SFA] with [MSA] = 10^6 molecules cm^{-3}, [MA] = 2.5 ×

732 10^8 molecules cm^{-3} and four different temperatures (green line: 298.15 K, blue line: 278.15 K, red

733 line: 258.15 K, black line: 238.15 K).

734

735

736 **Fig. 7** The J (cm^{-3} s^{-1}) (a) and R (b) as a function of [MSA] with [SFA] = 10^8 molecules cm^{-3} and

737 three different [MA] (black line: [MA] = 2.5 × 10^7 molecules cm^{-3}, red line: [MA] = 2.5 × 10^8

738 molecules cm^{-3}, blue line: [MA] = 2.5 × 10^9 molecules cm^{-3}) at 278.15 K.

739

740

741 **Fig. 8** Main cluster formation mechanism of MSA-MA-SFA-based system at 278.15 K, [MSA] =

742 10^7 molecules·cm^{-3}, [MA] = 2.5 × 10^8 molecules·cm^{-3}, and [SFA] = 10^6 molecules·cm^{-3}. (a) The

743 black arrows indicate the pure MSA-MA-based growth pathways. Blue arrows represent the

744 pathways containing SFA. The influence of (b) temperature, (c) [SFA] and [MSA] on the relative

745 contribution of the pure MSA-MA-based clustering pathway and the SFA participation pathway to

746 the system flux is analyzed. Others in (b), and (c) indicate that the pathway contribution of the

747 cluster growing out of the studied system is less than 5%

748
749
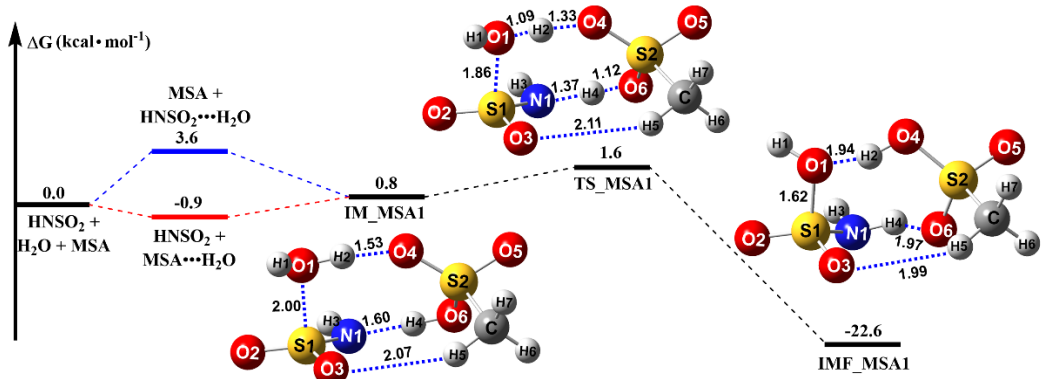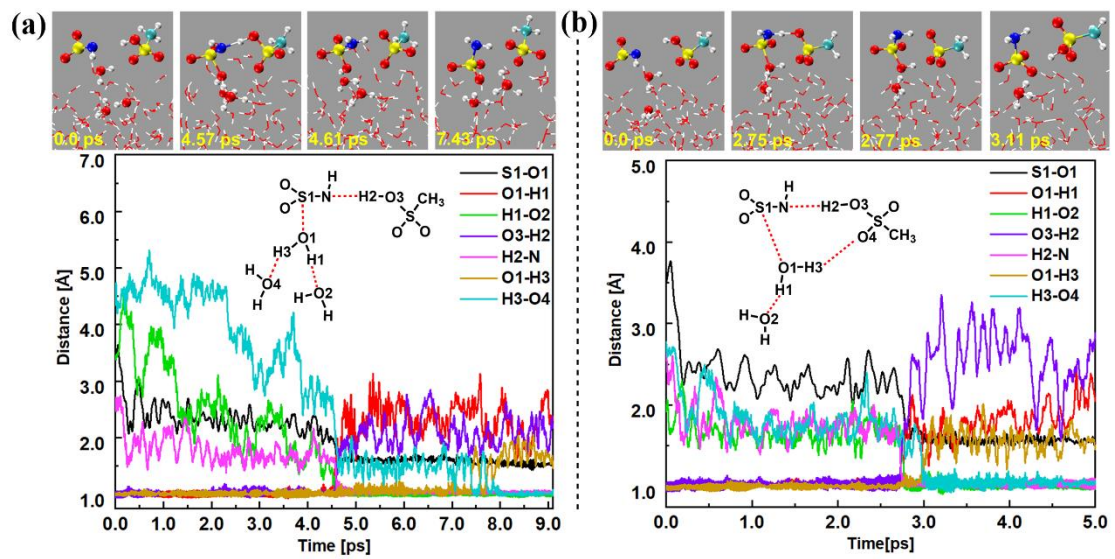
Fig. 1

Fig. 2

752

753

754

Fig. 3

Fig. 4

Fig. 5

757

758

759
760   Fig. 6

(a)

Cluster formation rate J (cm^{-3} s^{-1})
[SFA] = 10^8, T = 278.15 K

[MA] = 2.5 × 10^7 molecules·cm^{-3}
[MA] = 2.5 × 10^8 molecules·cm^{-3}
[MA] = 2.5 × 10^9 molecules·cm^{-3}

[MSA] (molecules·cm^{-3})

(b)

Enhancement strength R
[SFA] = 10^{8}molecules·cm^{-3}, T = 278.15 K

[MA] = 2.5 × 10^7 molecules·cm^{-3}
[MA] = 2.5 × 10^8 molecules·cm^{-3}
[MA] = 2.5 × 10^9 molecules·cm^{-3}

[MSA] (molecules·cm^{-3})

761

762   **Fig. 7**

31
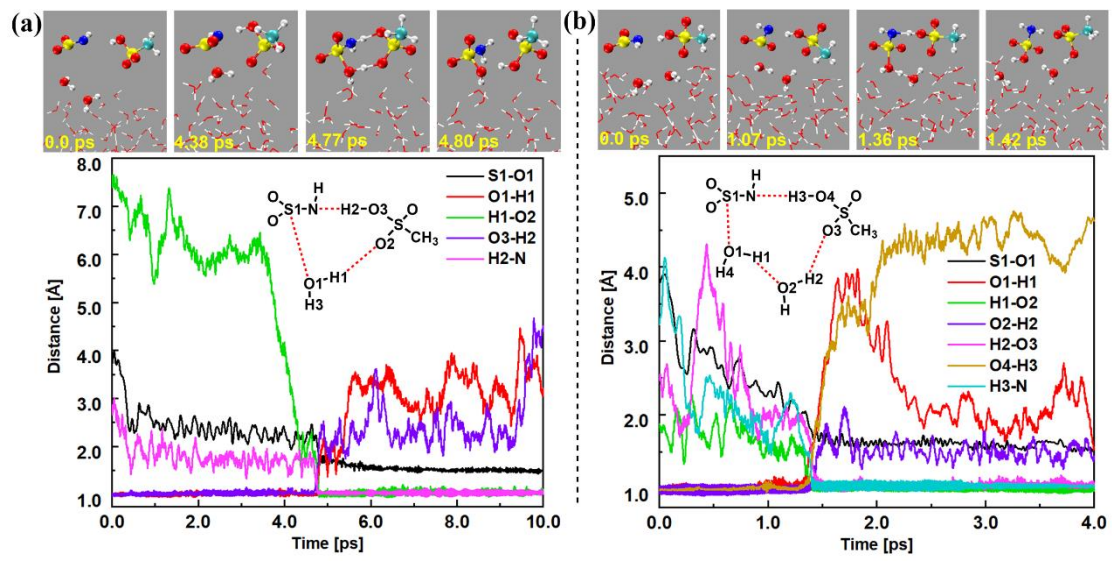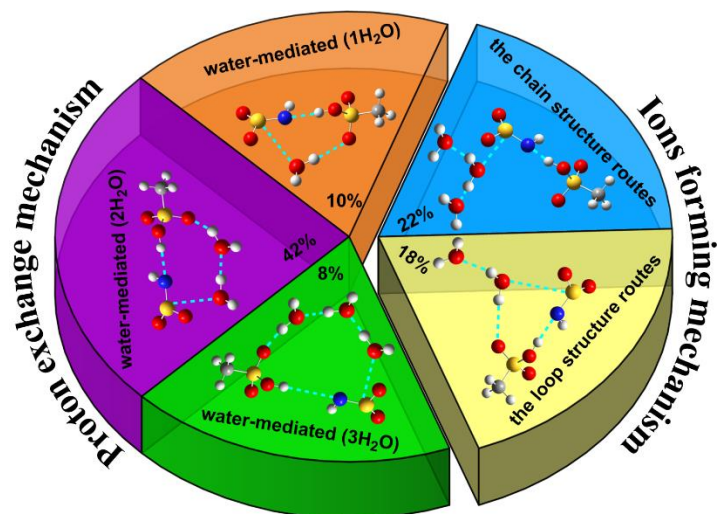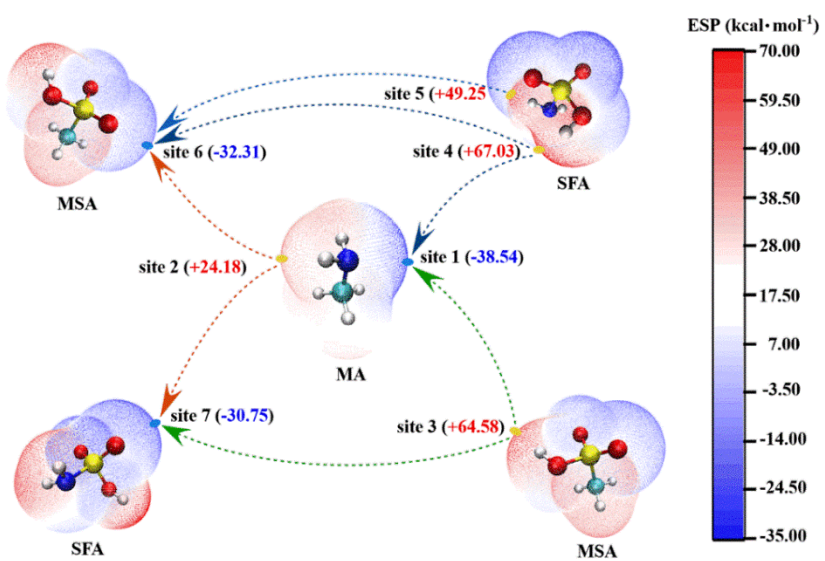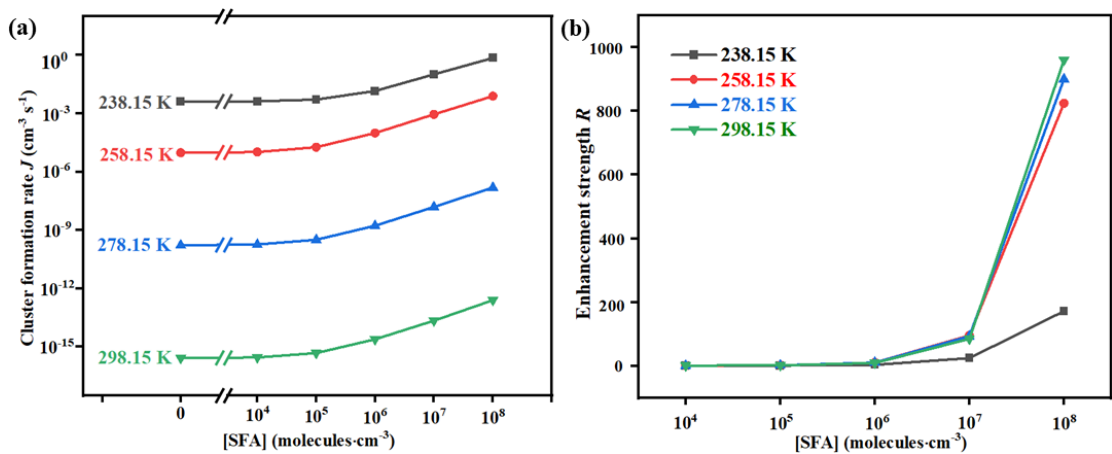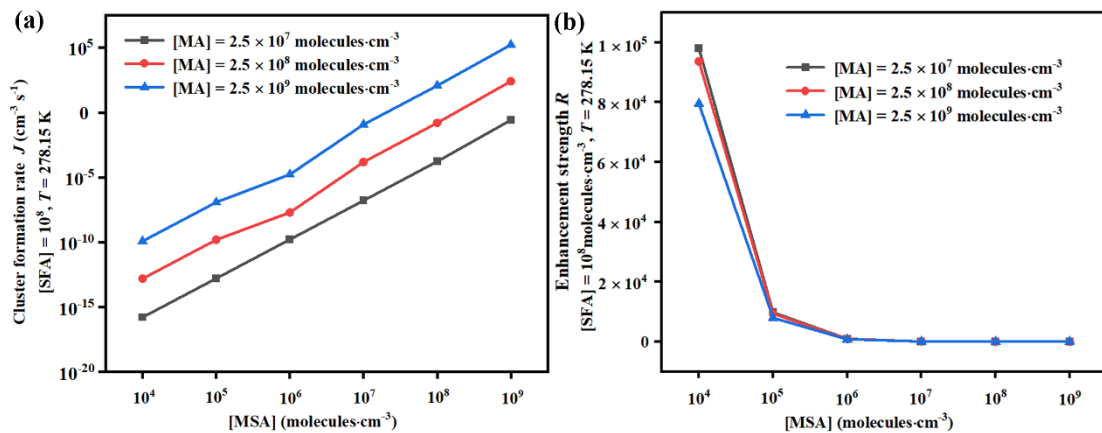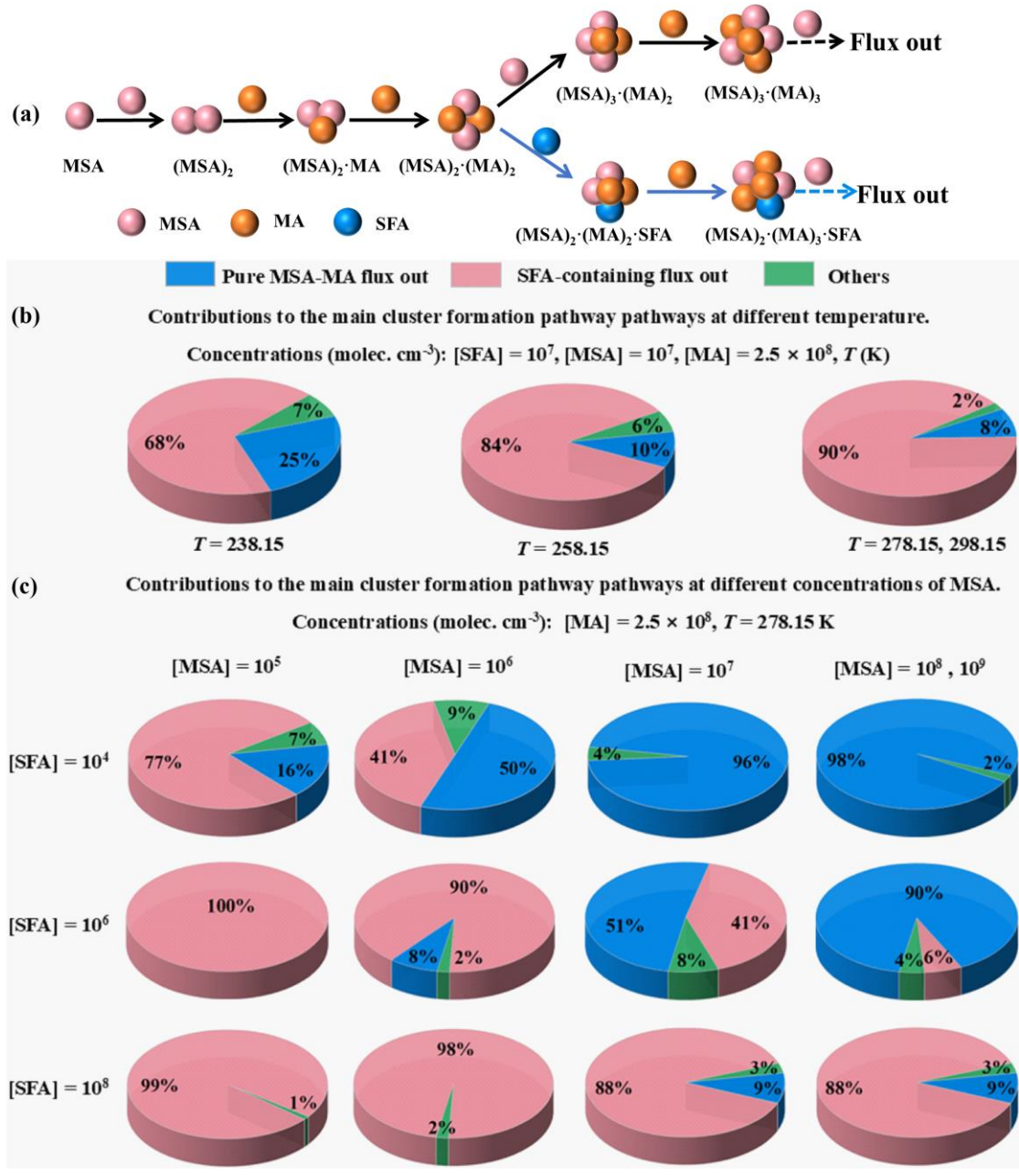
Fig. 8

Table 1 Rate coefficients (k, cm³·molecule⁻¹·s⁻¹) and effective rate constants (k', cm³·molecule⁻¹·s⁻¹) for the hydrolysis of HNSO₂ with H₂O and MSA calculated by master equation within the temperature range of 213-320 K and altitude range of 0-15 km

Altitude		0 km						5 km	10 km	15 km
T/K		280	290	298	300	310	320	259.3	229.7	212.6
k_{WM}		7.64×10^{-13}	6.45×10^{-13}	5.63×10^{-13}	5.44×10^{-13}	4.59×10^{-13}	3.88×10^{-13}	1.09×10^{-12}	1.72×10^{-12}	2.22×10^{-12}
k_{MSA}		3.08×10^{-11}	2.96×10^{-11}	2.85×10^{-11}	2.82×10^{-11}	2.67×10^{-11}	2.52×10^{-11}	3.32×10^{-11}	3.49×10^{-11}	3.50×10^{-11}
k'_{WM}	20%RH	5.99×10^{-18}	7.96×10^{-18}	9.64×10^{-18}	1.03×10^{-17}	1.29×10^{-17}	1.36×10^{-17}			
	40%RH	1.19×10^{-17}	1.58×10^{-17}	1.99×10^{-17}	2.07×10^{-17}	2.60×10^{-17}	3.12×10^{-17}			
	60%RH	1.79×10^{-17}	2.38×10^{-17}	2.98×10^{-17}	3.11×10^{-17}	3.90×10^{-17}	4.68×10^{-17}	9.85×10^{-27}	1.71×10^{-22}	6.51×10^{-22}
	80%RH	2.39×10^{-17}	3.17×10^{-17}	3.97×10^{-17}	4.14×10^{-17}	5.21×10^{-17}	6.24×10^{-17}			
	100%RH	2.97×10^{-17}	3.96×10^{-17}	4.97×10^{-17}	5.18×10^{-17}	6.50×10^{-17}	7.79×10^{-17}			
k'_{MSA}	[MSA]=10⁸	4.81×10^{-19}	2.50×10^{-19}	1.57×10^{-19}	1.40×10^{-19}	7.90×10^{-20}	4.60×10^{-20}	1.96×10^{-20}	2.37×10^{-19}	1.30×10^{-18}
k'_{MSA}/k'_{WM}		1.62×10^{-4}	6.42×10^{-5}	3.16×10^{-5}	2.69×10^{-5}	1.22×10^{-5}	5.90×10^{-5}	3.01×10^{1}	1.38×10^{3}	1.32×10^{8}

k_{WM} and k_{MSA} are respectively the rate constant for the hydrolysis of HNSO₂ with H₂O and MSA; k'_{WM} and k'_{MSA} are respectively the effective rate constant for the hydrolysis of HNSO₂ with H₂O and MSA.

Table 2. Gibbs free energy (ΔG) for the formation of SFA⁻···MSA, SFA⁻···NA, SFA⁻···OA, H₃O⁺···MA, MSA⁻···MSA, MSA⁻···OA, and MSA⁻···NA, MSA···MA, (MSA)₁·(MA)₁·(X)₁ at 298 K

	SFA⁻···MSA	SFA⁻···HNO₃	SFA⁻···OA	MSA⁻···MSA	MSA⁻···NA
ΔG	-23.8	-21.5	-25.2	-23.9	-22.6
	MSA⁻··· OA	MSA···H₃O⁺		MA···H₃O⁺	MSA···MA
ΔG	-25.8	-35.8		-57.9	-7.0 (-7.2)[b]
	HCOOH ···MSA···MA	CH₃COOH ···MSA···MA	CHOCOOH ···MSA···MA		OA ···MSA···MA
ΔG	-14.7 (-15.8)[a]	-14.8 (-14.3)[a]	-14.7 (-15.6)[a]		-13.3 (-12.7)[a]
	CH₃COCOOH ···MSA···MA	HOOCCH₂COOH ···MSA···MA	HOOC(CH)₂COOH ···MSA···MA		HOOC(CH₂)₂COOH ···MSA···MA
ΔG	-13.3 (-13.0)[a]	-14.7 (-16.7)[a]	-15.9 (-15.3)[a]		-13.9 (-14.3)[a]
	HOOC(CH₂)₃COOH ···MSA···MA	C₆H₅(COOH) ···MSA···MA	C₁₀H₁₆O₃ ···MSA···MA		SFA⁻ ···MSA···MA
ΔG	-18.9 (-17.9)[a]	-15.4 (-15.3)[a]	-16.4 (-15.3)[a]		-25.8

[a] The value was taken from reference (Zhang, R., Shen, J., Xie, H. B., Chen, J., and Elm, J.: The role of organic acids in new particle formation from methanesulfonic acid and methylamine, Atmos. Chem. Phys., 22, 2639-2650, 10.5194/acp-22-2639-2022, 2022b.)

[b] The value was taken from reference (Zhong, J., Li, H., Kumar, M., Liu, J., Liu, L., Zhang, X., Zeng, X. C., and Francisco, J. S.: Mechanistic Insight into the Reaction of Organic Acids with SO₃ at the Air–Water Interface, Angew. Chem. Int. Ed., 131, 8439-8443, 2019.)